vibration

MDPI

Article

Development of a Novel Magneto-Rheological Elastomer-Based Semi-Active Seat Suspension System

Yimei Wang, Hossein Vatandoost * and Ramin Sedaghati

Department of Mechanical, Industrial and Aerospace Engineering, Concordia University, Montreal, QC H3G 1M8, Canada; yimeiwang813@gmail.com (Y.W.); ramin.sedaghati@concordia.ca (R.S.)
* Correspondence: hossein.vatandoost@concordia.ca

Abstract: Human operators in the transportation sector are exposed to whole-body vibration (WBV) while driving. Occupational exposure to WBV, predominant at low frequencies (<20 Hz), has been linked to spinal injuries and reduced functioning. This study aims at the design development of a novel semi-active seat suspension system featuring magneto-rheological elastomers (MREs) to mitigate the WBV. The proposed suspension system allows a greater range of strokes, while ensuring the MRE remains within an acceptable level of deformation. Several MRE samples were fabricated and characterized under shear mode. Afterward, a field- and frequency-dependent phenomenological model was developed to predict the viscoelastic properties of MREs as functions of both the excitation frequency and applied magnetic field. The MRE material model was subsequently used to design and optimize an adaptive seat suspension system incorporating a C-shaped MRE-based isolator in parallel and series with passive springs. The proposed adaptive seat suspension system demonstrated a frequency shift of 29% by increasing the applied current from 0 to 2 A. Finally, a 6-DOF lumped parameter model of a seated human subject combined with the proposed semi-active suspension system featuring the MRE isolator has been formulated to investigate the vibration transmissibility from the floor to the subject's head.

Keywords: magneto-rheological elastomers (MREs); vibration isolator; seat suspension system; semi-active control; whole-body vibration

check for updates

Citation: Wang, Y.; Vatandoost, H.; Sedaghati, R. Development of a Novel Magneto-Rheological Elastomer-Based Semi-Active Seat Suspension System. *Vibration* **2023**, *6*, 777–795. https://doi.org/10.3390/vibration6040048

Academic Editor: Paul-Émile Boileau

Received: 6 August 2023
Revised: 19 September 2023
Accepted: 26 September 2023
Published: 29 September 2023

Copyright: © 2023 by the authors. Licensee MDPI, Basel, Switzerland. This article is an open access article distributed under the terms and conditions of the Creative Commons Attribution (CC BY) license (https://creativecommons.org/licenses/by/4.0/).

1. Introduction

Human operators in ground vehicles are generally exposed to low-frequency whole-body vibration (WBV) [1]. This is of primary concern as the human body is at its most sensitive in the low frequency range (3–12 Hz) [2,3]. The suppression of WBV-induced injuries to human operators in transportation has been a challenging task owing to varied aspects related to seated occupant compliance, anthropometry, and vibration conditions [4,5]. Typically, three types of vibration isolators have been developed to date, namely, passive, semi-active, and active systems for the mitigation of vibration transmitted to the human body [6]. The passive systems are capable of providing vibration isolation over a limited frequency range which has been specified at an early design stage. Mistuned conditions, however, can adversely affect the performance of passive systems. Active systems can provide a significant performance gain compared with passive systems; however, they suffer from instability and large power consumption as well as complex control hardware [7]. Semi-active systems, on the other hand, can provide the reliability and fail-safe feature of the passive systems while relatively maintaining the adaptability of the fully active systems [8,9].

There have been various reported studies for semi-active and active seat suspension systems utilizing magneto-rheological (MR) fluids with adjustable damping properties to mitigate the negative effects of transmitted vibration on seated occupants [10–15]. However, limited studies have focused on the development of semi-active seat suspension systems

based on MR elastomers (MREs), which can simultaneously change their damping and stiffness properties. Dushchenko et al. [16], for instance, developed a suspension lever hinge that incorporates MREs and assessed their variable stiffness and damping characteristics. They reported a 40% increment in the ride smoothness of the wheeled vehicle. The majority of research conducted in this field has primarily focused on using the negative stiffness properties of MREs for horizontally isolating seats from induced vibrations; this is because the low-frequency WBV cannot be effectively isolated by most passive suspensions in typical seats [17]. However, there has been limited investigation into the vertical vibration isolation of seats using MRE-based vibration isolators, particularly when considering a low frequency range and large strokes. For instance, Sun et al. [18] presented the design development and control of an MRE-based semi-active seat suspension system working in horizontal mode. Their design possessed an MRE isolator system consisting of two permanent magnets and an electromagnetic coil to realize the negative stiffness, and they demonstrated that the ride comfort of the MRE isolator-based seat suspension is significantly better than the passive seat suspension. Also, Choi et al. [19,20] investigated the effectiveness of an MRE-based dynamic vibration absorber in mitigating WBV in vertical mode but under a high-frequency range (100–250 Hz). Li et al. [21] and Du et al. [22], respectively, developed and simulated the control of an MRE-based seat suspension in vertical mode. However, its practical implementation might require a full-scale MRE isolator that can handle the intended tasks, such as supporting the weight of a human body while preventing significant deformation of the MREs. This can pose challenges in predicting and controlling the behavior of MREs when subjected to large deformations.

The limited research on MRE-based semi-active vibration seat suspension system working in low-frequency vertical mode is mainly attributable to the fact that the stiffness of seat suspensions is required to be designed as soft as possible to have a lower natural frequency (ω_n) than the excitation frequencies of interest, thereby providing superior vibration isolation above $\sqrt{2}\omega_n$ [20]. At the same time, a large stiffness is required to avoid excessive deflection due to the seated occupant's weight. For instance, Liu et al. [23] developed an MRE-based semi-active seat suspension to provide vertical vibration isolation for seat applications. To avoid the nonlinear strain softening behavior of MRE materials at large deformations, a low stroke limit of 5 mm was considered in their design, which may limit their practical application for seat suspensions that normally require 1–10 cm deformation. It should be noted that utilizing larger strokes instead of smaller strokes can reduce the amount of force transmitted to the human body, particularly in the case of shock loadings.

Despite the fact that this classical trade-off between isolation and static displacement in vertical mode is well known [24], studies have hardly ever utilized an MRE-based seat suspension system to tackle this problem. To address the above-mentioned trade-off, in the present study a novel semi-active seat suspension system employing an MRE-isolator unit together with parallel and series passive springs has been proposed. A design optimization problem has been formulated to identify the optimal parameters of the proposed semi-active suspension system which integrates an MRE isolator in parallel and series with passive springs. The design optimization was realized using a developed field- and frequency-dependent phenomenological model for MREs under shear mode. The proposed semi-active suspension system based on MREs (i) can allow a large vertical deformation of the seat while maintaining MREs to operate within a limited deformation regime, and (ii) provides sufficient frequency shift/vibration isolation.

2. Fabrication, Characterization, and Modeling of MREs

Designing smart devices based on MRE materials requires a robust material model capable of capturing the MRE dynamic behavior under both the magnetic field and mechanical deformation. The model can be subsequently used for modeling and design optimization of MRE-based devices. To develop such a material model, it is indeed necessary to first characterize MRE dynamic behavior experimentally under relatively wide ranges

of magnetic and mechanical loadings. The characterization can be implemented in shear and tension/compression loading configurations. Since the shear mode operation of MREs requires much simpler configuration in terms of both the design of the magneto-mechanical device and the characterization procedure, the present study is mainly concerned with the shear mode characterization of MREs using an advanced magneto-rheometer, as shown in Figure 1a.

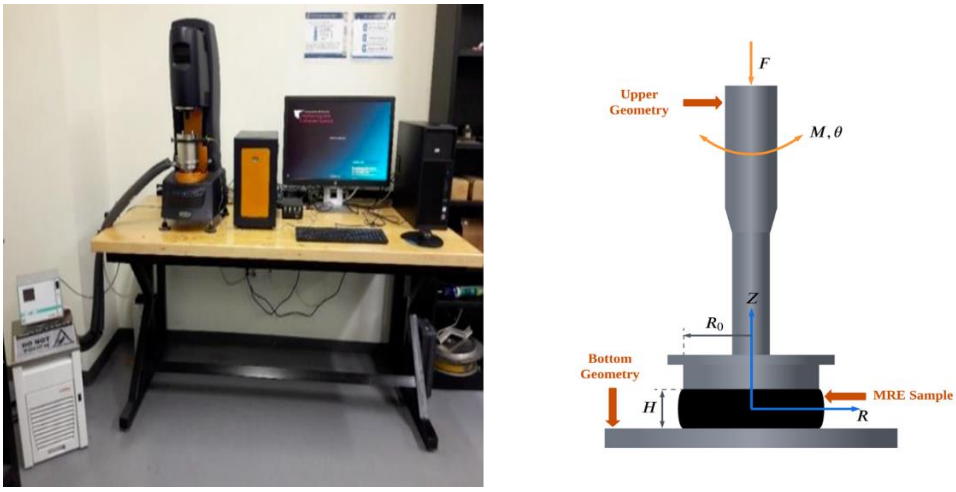

(**a**) (**b**)

Figure 1. MREs testing system. (**a**) The MREs testing system; (**b**) schematic diagram of the rotational parallel-plate setup of the rotary rheometer equipped with magneto-rheology accessory.

To implement the characterization of MREs in shear mode, an isotropic MRE batch was fabricated in the laboratory for the sake of convenience, and it would be sufficient to establish the proof-of-concept of a semi-active seat suspension system based on MRE materials. It should be noted that the anisotropic MREs will generally lead to a higher magneto-rheological effect, but optimizing the performance of MRE materials and devices is not the prime focus of the current study. Succinctly, magnetically soft carbonyl iron particles (referred to as CIPs with SQ-grade, BASF Co., Ludwigshafen, Germany) were initially mixed with liquid silicone rubber (Eco-flex 00-20 series, Smooth-On, USA) for several minutes at laboratory temperature (20 °C). The average diameter of CIPs varies from 3.9 to 5 µm. It should be noted that the volume concentration of the MRE sample was selected as 25% to maximize the MR effect. After thoroughly mixing the CIPs with silicone rubber, the mixture was degassed using a vacuum chamber until a negative pressure of 29 in-Hg was realized, thereby removing any potential air bubbles from the mixture. Then, the mixture was poured into a cylindrical mold with a diameter and thickness of 80 mm and 1 mm, respectively. The MRE was then allowed to be cured at laboratory temperature (20 °C) for 24 h. Since no magnetic field was supplied while curing the sample, the fabricated MRE had an isotropic microstructure in which the magnetizable particles were randomly distributed within the rubber-like matrix. Subsequently, cylindrical MRE samples with a diameter of 20 mm were cut from the fabricated batch, which is suitable for characterization with the commercially available magneto-rheometer shown in Figure 1. An advanced magneto-rheometer device (Discovery HR-3, TA instrument Co., New Castle, DE 19720, USA) equipped with an electromagnet cell was used for characterization, as shown in Figure 1a. A schematic diagram of the rotational parallel plate configuration with the MR unit attachment is shown in Figure 1b. In this figure, F, M, θ, R_0, Z, R, and H, respectively, represent vertical static force applied on MRE sample, applied torque, rotational angle, diameter of standard sample, vertical axis, radial axis, and thickness of MRE sample. To prevent slippage during the test, the MRE sample was clamped between the upper and lower geometry with an axial preload of around 10 N. The MR unit produces a consistent and uniform magnetic flux density up to 1 Tesla along the axis of the cylindrical

MRE sample, perpendicular to the direction of shear motion. The magnetic flux density is measured by a Hall probe sensor, which is located directly below the MRE sample.

In this study, we employed an advanced magneto-mechanical test rig equipped with the rotary rheometer shown in Figure 1, to conduct the characterization of the MRE samples in shear mode. Figure 1b shows the parallel-plate part of the rheometer which requires a cylindrical sample to apply the oscillatory torque. A series of experiments were subsequently conducted under varied mechanical and magnetic loadings (loading frequency and strain amplitude). The input mechanical loading was sinusoidal with a frequency ranging from 0.2 Hz to 10 Hz under the strain amplitudes of 15% and 30%. As mentioned before, prior to the application of sinusoidal oscillation, a pre-load of 10 N was applied to not only prevent the MRE samples from slipping at a higher frequency but also to represent a real and practical situation which MREs experience in applications. The magnetic field was realized by the embedded electromagnetic unit within the MR cell. The value of magnetic flux density for characterization varied from 0 T to 1.0 T. It should be noted that the TA instrument was equipped with a temperature unit control that kept the temperature of the sample near 20 °C during the characterization tests. The experiments were selectively repeated at least two times in order to ensure the repeatability of the recorded data. The repetition was performed for all data due to the time-consuming task of each experiment to be implemented by the rheometer. Relatively consistent results were observed and recorded. Figures 2 and 3 show the experimental data of MRE samples under shear mode in terms of shear storage (G') and loss (G'') moduli at a strain amplitude of 30% and 15%, respectively. The results in Figure 2, for example, are concern the strain amplitude of 30% under varied loading frequencies. The results show the variation of these moduli with respect to the magnetic field intensity. Increasing the field intensity yielded an increment in both shear moduli irrespective of the loading frequency, which are generally referred to as field stiffening and field dampening effects, respectively [25]. However, the values of the storage modulus were consistently higher than those of the loss modulus, confirming the fact that the MRE materials display a less viscoelastic and more elastic behavior. Such a tendency has also been observed in [26]. The G' and G'' vary nearly in linear manner with respect to the magnetic flux density and then show a nonlinear behavior as the magnetic flux density increases toward the saturation limit. The field stiffening effect becomes less pronounced for higher frequencies due to the strain-rate stiffening phenomenon, in which elastomeric materials become stiff at higher rates of deformation, as can be observed in Figure 2a. For instance, under the magnetic flux density of 0.6 T, the storage modulus varied from 108 kPa to 121 kPa when the loading frequency was increased from 2 Hz to 10 Hz, respectively. However, the field-dampening effect is relatively independent of the loading frequency, as shown in Figure 2b.

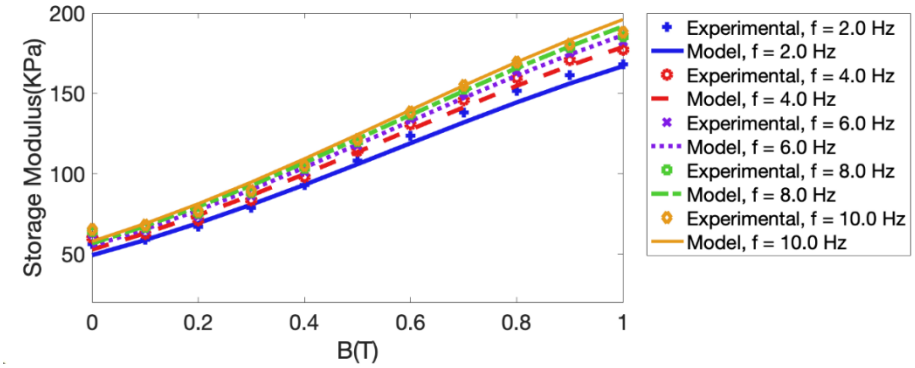

(**a**)

Figure 2. *Cont.*

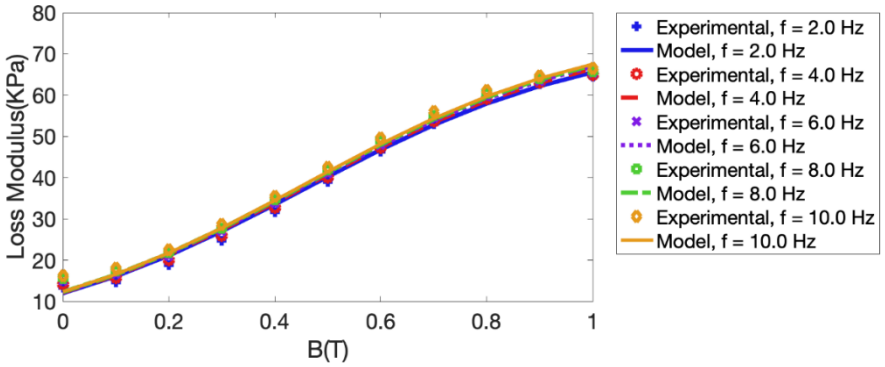

(**b**)

Figure 2. Variation of the experimentally obtained storage and loss moduli at a strain amplitude of 30% with respect to the magnetic flux density under different loading frequencies. The graph also illustrates the model-predicted MRE moduli. (**a**) Storage modulus; (**b**) Loss modulus.

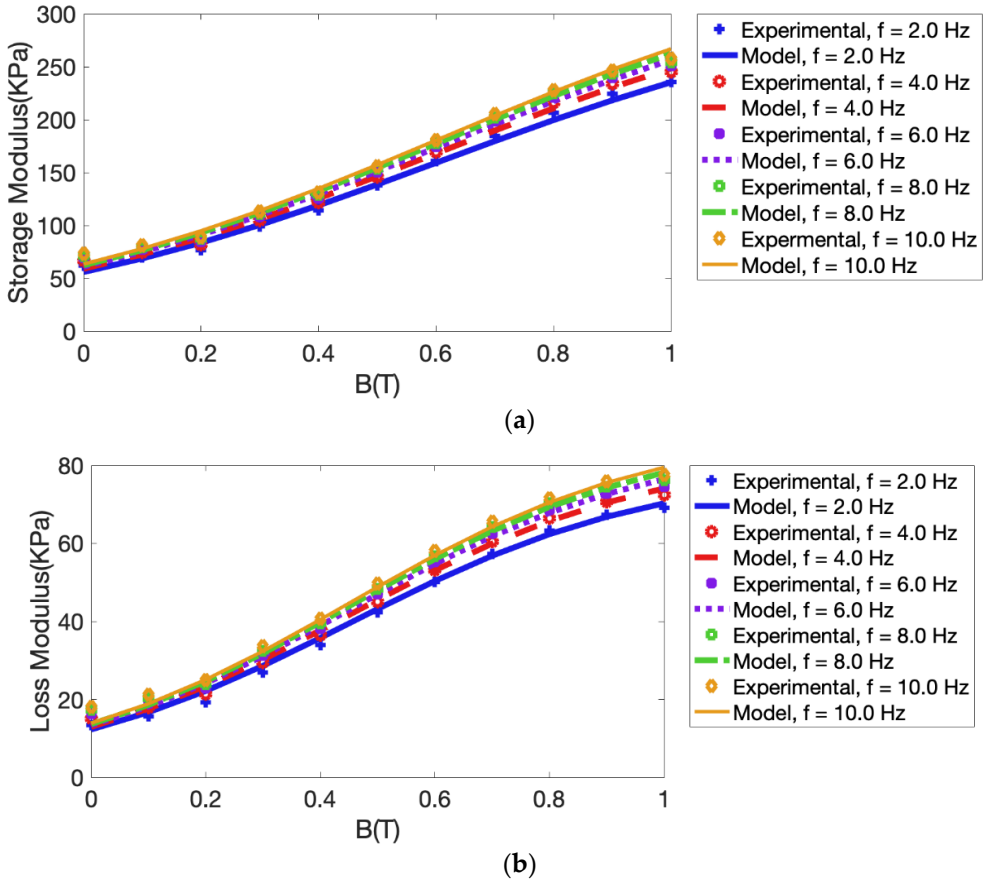

(**a**)

(**b**)

Figure 3. Comparison of storage and loss modulus prediction models with experimental data (strain amplitude 15%). (**a**) Storage modulus (**b**) Loss modulus.

Moreover, Figure 2 further shows that G'' has more tendency to saturate as compared with G' when the magnetic flux density exceeds 0.8 T. This is also observed in another study on characterization of magneto-mechanical behavior of MREs [26]. In [26], the experimental characterization was performed under a loading frequency of 10 Hz and a strain amplitude of 1% considering flux density varying from 0 to 800 mT; as an example, under a flux density of 600 mT and a loading frequency of 10 Hz, the storage modulus was reported as 500 kPa, while in this study, under the same loading frequency and flux density, the storage moduli of nearly 170 kPa and 121 kPa were obtained under a strain amplitude of 15% and

30%, respectively. This comparison confirms the strain softening phenomenon in which MRE materials become soft as the strain amplitude increases.

Phenomenological models are subsequently developed to predict the viscoelastic properties of the tested MREs as a function of the loading frequency and magnetic flux density. Based on the observed results, the variation of the MRE's storage G' and loss G'' moduli with respect to the driving frequency can be represented by a combination of exponential and power functions, as presented in Equations (1) and (2). It is important to note that the selected exponential function for the magnetic field can represent the magnetic saturation of the MRE modulus at high magnetic field intensities. Hence, the mathematical models for the storage and loss moduli may be formulated as:

$$G\prime(B,f) = \frac{2a_1 f^{a_2}}{1+e^{(-a_3(B+a_4))}} \tag{1}$$

$$G''(B,f) = \frac{2b_1 f^{b_2}}{1+e^{(-b_3(B+b_4))}} \tag{2}$$

where G' and G'' represent the storage and the loss moduli, respectively, and both are functions of the magnetic flux density (B) and excitation frequency (f). a_1, a_2, a_3, a_4 and b_1, b_2, b_3, b_4 are the model's characteristic parameters to be determined through an error minimization procedure. In order to obtain the parameters of the proposed model, the error functions are first defined as:

$$J_{G'} = \sum \left(G'_{model} - G'_{expire}\right)^2 \tag{3}$$

$$J_{G''} = \sum \left(G''_{model} - G''_{expire}\right)^2 \tag{4}$$

By using the least squares minimization method, the model parameters have been identified to minimize the above-mentioned error functions. The above-mentioned procedure was repeated for a strain amplitude of 15% and 30%. The obtained parameters are provided in Tables 1 and 2 for a strain amplitude of 15% and 30%, respectively.

Table 1. Identified parameters (strain 15%).

a_1	a_2	a_3	a_4
$\mathbf{1.523 \times 10^5}$	0.078	2.562	−0.608
b_1	b_2	b_3	b_4
$\mathbf{3.760 \times 10^4}$	0.077	3.751	−0.452

Table 2. Identified parameters (strain 30%).

a_1	a_2	a_3	a_4
$\mathbf{1.066 \times 10^5}$	0.099	2.290	−0.563
b_1	b_2	b_3	b_4
$\mathbf{3.692 \times 10^4}$	0.018	3.615	−0.458

Figure 2 also compares the experimentally derived MRE moduli and model-predicted storage and loss moduli for different loading frequencies and magnetic flux densities under a strain amplitude of 30%. The results show that the proposed model can effectively predict the behavior of MRE moduli as a function of both the loading frequency and magnetic flux density. A relatively good agreement was observed between the model and experimental results within the entire range of magneto-mechanical loading conditions considered. For instance, Figure 3 shows the performance of the proposed model in the prediction of the storage and loss moduli for different loading frequencies and magnetic flux densities for a

loading amplitude of 15%. Results show that the proposed model can effectively predict the behavior of MRE moduli as a function of both the loading frequency and magnetic flux density.

The comparison of the results presented in Figures 2 and 3, associated with a strain amplitude of 30% and 15%, respectively, confirms the strain-softening phenomenon that the higher the strain amplitude, the softer the material. Figure 4 also compares the results for the storage and loss moduli versus frequency under different magnetic flux densities obtained using the proposed model and experimental results for a strain amplitude of 30%. The results again show a very good agreement between the model and experimental results. Figures 4 and 5 further compare the results obtained by the proposed model and the experimental results, when the storage and loss moduli are varied with respect to loading frequency for a strain amplitude of 30% and 15%, respectively. The comparison also was applied to all levels of magnetic flux densities, ranging from 0 T to 1 T.

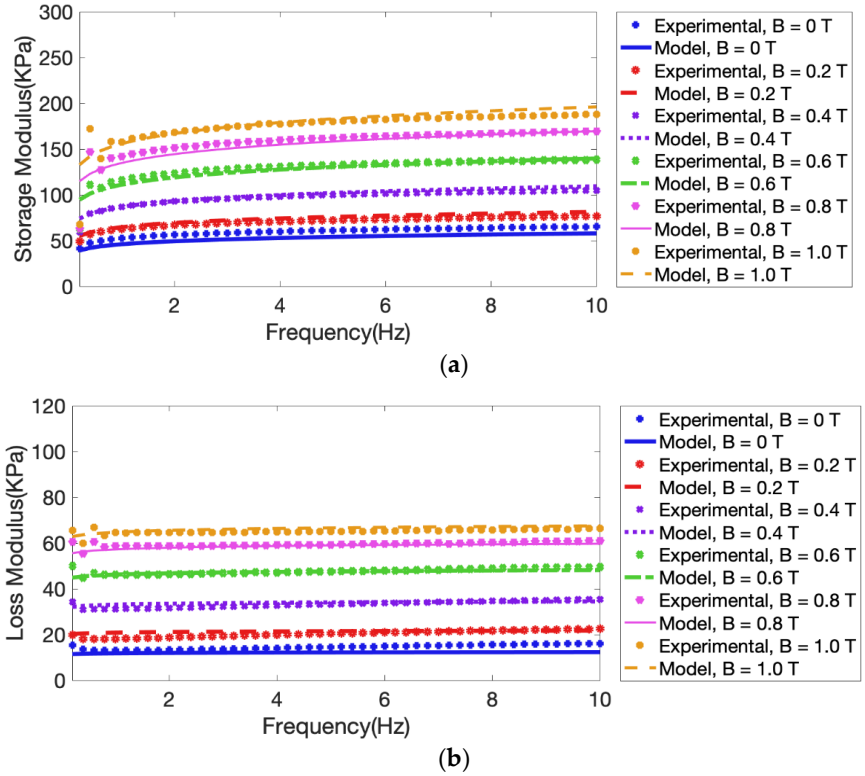

(**a**)

(**b**)

Figure 4. Variation of the experimentally obtained storage and loss moduli with respect to loading frequency under different magnetic flux densities. The graph also shows the model-predicted MRE moduli (strain amplitude 30%). (**a**) Storage modulus; (**b**) Loss modulus.

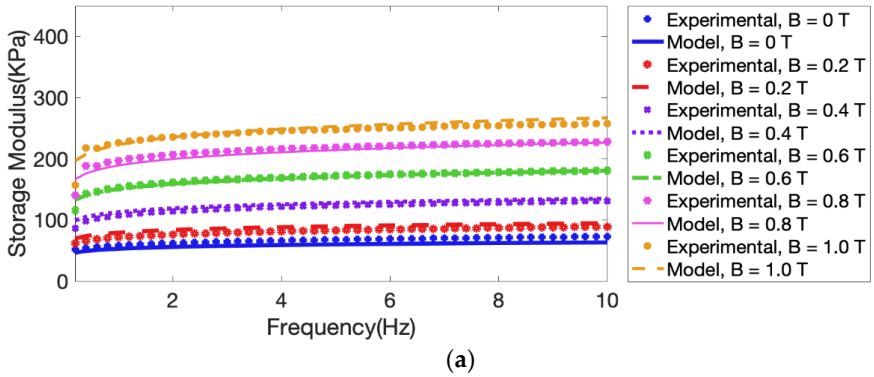

(**a**)

Figure 5. *Cont.*

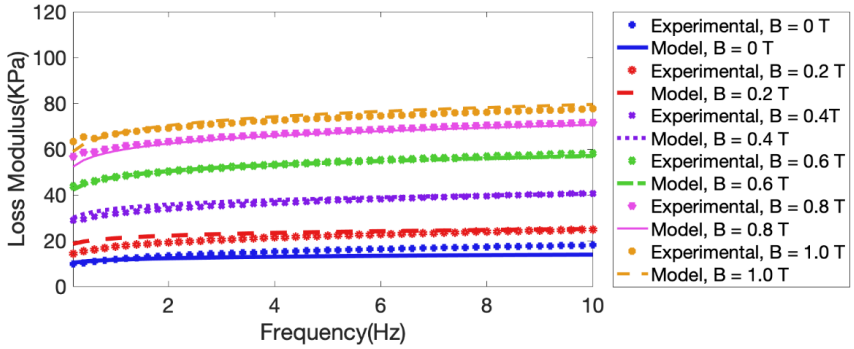

(**b**)

Figure 5. Variation of the experimentally obtained storage and loss moduli with respect to loading frequency under different magnetic flux densities. The graph also shows the model-predicted MRE moduli (strain 15%). (**a**) Storage modulus; (**b**) Loss modulus.

Apart from a qualitative comparison between the model-predicted MRE moduli and the corresponding experimental data, presented in Figures 2–5, Tables 3 and 4 provide a quantitative comparison between the model and experimental data. There is a relatively acceptable level of relative errors for the developed frequency- and field-dependent phenomenological models.

Table 3. Comparison of experimental data vs. predicted model (strain 30%).

30%	*Storage Modulus* (KPa)			*Loss Modulus* (KPa)		
Applied Filed (T)	Experimental Data	Predicted Model	Error (%)	Experimental Data	Predicted Model	Error (%)
B = 0	52.6	46.0	12.5	13.0	11.8	9.2
B = 0.2	62.7	64.7	3.2	18.2	20.9	14.8
B = 0.4	87.0	86.9	0.1	31.2	33.1	6.1
B = 0.6	115.9	111.1	4.1	46.2	46.2	0
B = 0.8	141.6	134.8	4.8	58.8	57.2	2.7
B = 1.0	157.8	155.9	1.2	64.5	64.7	0.3

Table 4. Comparison of experimental data vs. predicted model (strain 15%).

30%	*Storage Modulus* (KPa)			*Loss Modulus* (KPa)		
Applied Flux Density (T)	Experimental Data	Predicted Model	Error (%)	Experimental Data	Predicted Model	Error (%)
B = 0	58.5	53.0	9.4	11.8	11.7	0.8
B = 0.2	71.8	79.2	10.3	17.4	21.0	20.6
B = 0.4	107.4	112.7	4.9	31.8	33.9	6.6
B = 0.6	153.1	150.7	1.5	47.8	47.8	0
B = 0.8	197.1	189.0	4.1	60.6	59.2	2.3
B = 1.0	226.2	222.9	1.4	66.6	66.7	0.1

Figure 6 shows that the MRE material becomes soft as the strain amplitude increases from 15% to 30%, irrespective of the applied frequency and magnetic flux density, due to strain softening or Payne effect. For instance, under a frequency of both 4 Hz and 10 Hz and all values of the applied flux density from 0 to 1 Tesla, the MREs are stiffer at 15% as compared with 30% strain amplitude. However, to develop a semi-active suspension

system that could deal with real-world scenarios where the seat might experience a larger level of displacements, we select the material model developed for the strain amplitude of 30% in order to design the seat in the subsequent sections.

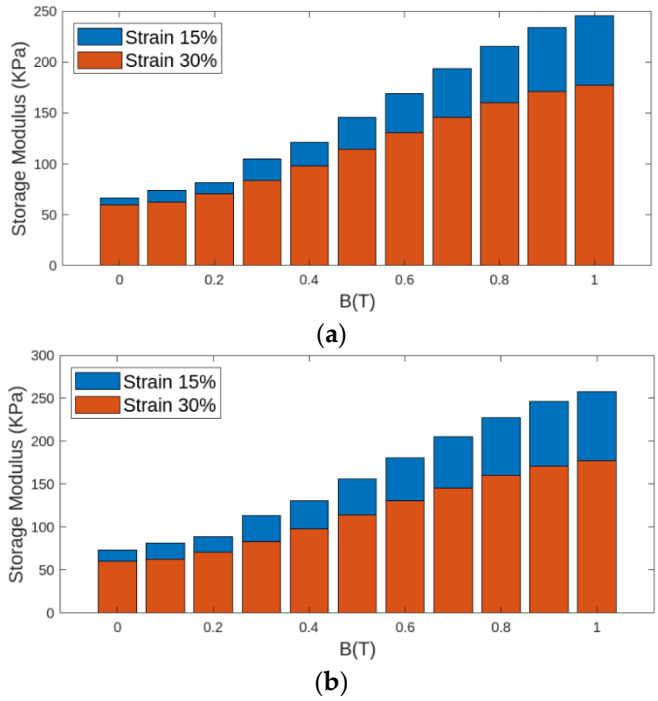

Figure 6. Variation of the storage modulus with respect to applied flux density under different loading frequencies: (**a**) 4 Hz; (**b**) 10 Hz.

3. Design Optimization of MRE-Based Vibration Isolator

This section presents a design optimization of a novel MRE-based vibration isolator that can be simply integrated for the subsequent design development of the proposed seat suspension systems. MREs show many potentials for applications in noise and vibration control, such as MRE isolators and MRE absorbers, due to their variable stiffness and damping properties under the application of an external magnetic field. However, as compared with MR fluids, MREs demand relatively larger and bulkier electromagnet units to magnetically activate them, as their total designed thickness is normally much higher than that of MR fluids. Thus, designing an optimal electromagnetic unit which can provide enough magnetic field in the MRE active regions with minimal mass and space remains a continuous challenge in this field and thus needs to be properly addressed. In this section, therefore, the design optimization of an MRE-based vibration isolator equipped with a C-shaped electromagnet is presented.

The schematic of the proposed MRE isolator with all important design parameters is shown in Figure 7. The MRE isolator mainly consists of four parts: (i) a connector that connects the seat to the MRE samples from the upper section, (ii) a C-shape steel core, (iii) two electromagnet coils, and (iv) two cuboid-shaped MRE samples under shear mode located in air gap. The geometrical parameters of the isolator are presented using parameters x_1 to x_6, as shown in Figure 7. H_{total}, D_{total}, and W_{total} represent the total height, depth and width of the designed C-shaped electromagnet. It should be noted that x_c (thickness of the plate connecting the MREs to the connector) is assumed to be 20 mm. To design an electromagnetic circuit for an MRE-based isolator, it is required to maximize the magnetic flux density within MRE specimens in the gap of the electromagnet while limiting the space, mass, and energy consumption of the isolator unit. At the same time, the off-state modulus of MREs should be sufficient enough to withstand the weight of the human operator on the seat. More importantly, the electromagnet unit should be able to

operate for a sufficient amount of time while avoiding an extreme temperature rise that could damage the coil. The simultaneous consideration of such important requirements has mostly been ignored in the previous design of MRE systems.

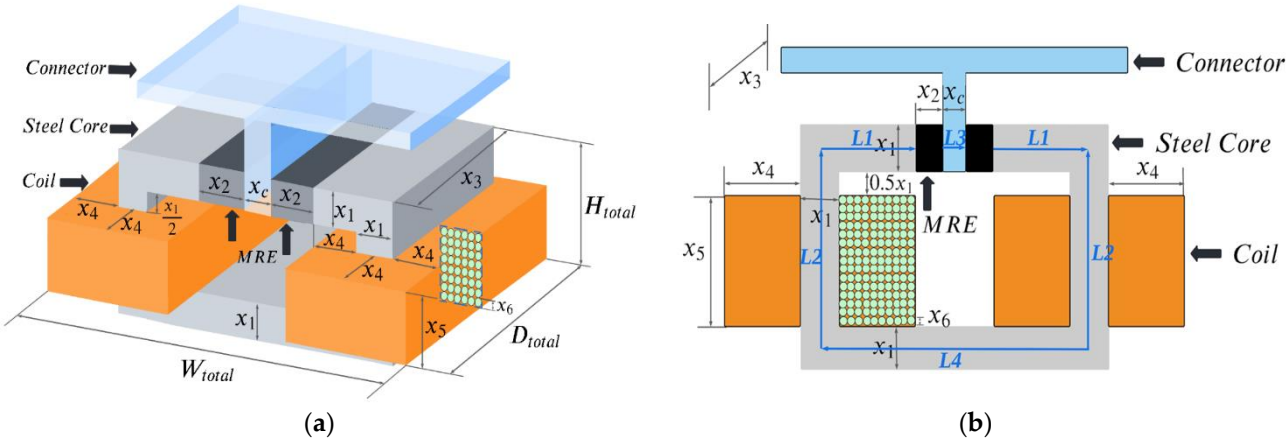

Figure 7. Schematic of the designed MRE isolator: (**a**) 3D view, and (**b**) 2D view.

The cross-section of copper conductors is schematically shown in green as depicted in Figure 7. To implement the above-mentioned design optimization of the MRE isolator, the geometrical and physical parameters of the isolator unit should be related together using Hopkinson's law (equivalent to Ohm's law in electrical circuits) as follows [27]:

$$\oint H.dl = NI = \mathcal{R}_t \phi \tag{5}$$

where H and l are the applied magnetic field and length of the mean magnetic path of the core. N, I, $\mathcal{R}_t$, and ϕ are the total number of copper wire turns, applied electrical current, total reluctance of the circuit, and the magnetic flux in the air gap of the C-shaped core. Substituting the reluctance of different parts of the electromagnet circuit in Equation (5) yields:

$$NI = \phi(2\mathcal{R}_{MRE} + \mathcal{R}_{core}) \tag{6}$$

The reluctances of the magnetic core and MRE can be calculated as $\mathcal{R}_{core} = l_{core}/(\mu_{core}A_{core})$, and $\mathcal{R}_{MRE} = l_{MRE}/(\mu_{MRE}A_{MRE})l_{core}$, A_{core}, and μ_{core} are the length of steel core, cross-sectional area, and permeability. These can be similarly defined for MRE magnetic materials. As can be seen in Figure 7, the cross-sectional areas of the core and MRE are the same, $A_{core} = A_{MRE}$. The number of coil turns can be approximated as follows [27]:

$$N = 2(f_w x_4 x_5 / A_{wire}) \tag{7}$$

where f_w is the practical filling factor of 0.8 when wrapping the conductor wire around the bobbin core. $A_{wire} = \pi {x_6}^2/4$ is the cross-sectional area of the conductor wire and x_6 is the diameter of the conductor wire. Moreover, considering the continuity of the flux within a closed path magnetic circuit, the magnetic flux can be calculated as a multiplication of the magnetic flux density of the MRE with its cross-sectional area:

$$\phi_{MRE} = B_{MRE}A_{MRE} = B_{MRE}x_1x_3 \tag{8}$$

The aim is to maximize the magnetic flux density (B_{MRE}) passing through the electromagnet air gap filled with the MRE specimens. Considering Equations (5)–(8), B_{MRE} can be calculated as follows:

$$B_{MRE} = \frac{NI}{\frac{1}{\mu_0}\left(\frac{2l_{MRE}}{\mu_{r_{MRE}}} + \frac{l_{core}}{\mu_{r_{core}}}\right)} \tag{9}$$

where μ_0 is the vacuum permeability $(4\pi \times 10^{-7}\ H/m)$. $\mu_{r_{MRE}}$ and $\mu_{r_{core}}$ are, respectively, the relative magnetic permeability of the MRE and steel core materials, the values of which are assumed to be around 3 and 1000, respectively [28]. Using Figure 7b, the length of the steel core, l_{core}, and MRE, l_{MRE}, can be evaluated as follows:

$$l_{core} = 2L_1 + 2L_2 + L_3 + L_4 \tag{10}$$

$$L_1 = 0.5x_1 + x_4 \tag{11}$$

$$L_2 = x_5 + 2 \times 0.5x_1 + 0.5x_1 \tag{12}$$

$$L_3 = x_c \tag{13}$$

$$L_4 = x_c + 2L_1 + 2x_2 \tag{14}$$

$$l_{MRE} = 2x_2 \tag{15}$$

Substituting Equations (11)–(14) into Equation (10) yields:

$$l_{core} = 5x_1 + 2x_2 + 4x_4 + 2x_5 + 2x_c \tag{16}$$

The optimization can be formally formulated as:

$$\text{Minimize: } J(\theta) = -B_{MRE} \tag{17}$$

where B_{MRE} is the magnetic flux density induced in the MRE region at the maximum applied current of 2 A calculated using Equation (9), and θ is the design parameters defined as:

$$\theta = [x_1, x_2, x_3, x_4, x_5, x_6] \tag{18}$$

subjected to the following physical, geometrical, and design requirements of the seat suspension as:

$$\begin{gathered} 100\text{ mm} \leq H_{total} \leq 280\text{ mm} \\ 100\text{ mm} \leq W_{total} \leq 400\text{ mm} \\ 100\text{ mm} \leq D_{total} \leq 150\text{ mm} \\ 5\text{ kg} \leq M_{total} \leq 25\text{ kg} \\ 2.5\text{ kN/m} \leq k_{MREoff-state} \\ 20\text{ kN/m} \leq k_{MREon-state} \\ CD \leq 5 \end{gathered} \tag{19}$$

Where H_{total}, W_{total}, and D_{total} are the total height, width, and depth of the MRE isolator device (constraint volume), respectively, as shown in Figure 7. M_{total} is the total mass of the MRE isolator, and CD is the current density passing through the coil. $k_{MREoff-state}$ and $k_{MREon-state}$ are the total quasi-static stiffness of the MREs under zero and maximum magnetic flux densities, respectively. The lower and upper bound of stiffness were selected to minimize the frequency average (rms) weighted acceleration input to the human based on the standard ISO 2631/1:1997 [29,30]. Considering the schematic of the MRE under shear mode shown in Figure 8 and the shear storage modulus of the MRE in Equation (1), the equivalent stiffness of the MRE can be estimated as follows:

$$k_{MRE} = \frac{G'(B,\omega)A_{MRE}}{l_{MRE}} = \frac{G'(B,\omega)x_1x_3}{2x_2} \tag{20}$$

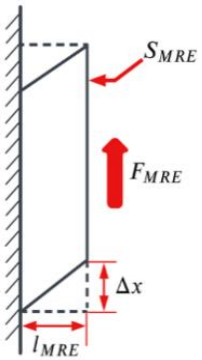

Figure 8. Schematic of the MRE under shear mode.

In similar, the equivalent damping of MREs can be also related to the shear loss moduli, presented in Equation (2), as follows:

$$c_{MRE} = \frac{G''(B,\omega)A_{MRE}}{\omega l_{MRE}} = \frac{G''(B,\omega)x_1x_3}{\omega 2x_2} \tag{21}$$

The genetic algorithm (GA) was initially used to obtain the near-global minimum solution due to the stochastic nature of the GA algorithm. The sequential quadratic programming (SQP) algorithm was subsequently used in which the optimal parameters from GA were used as initial inputs. SQP is a nonlinear gradient-based optimization algorithm capable of accurately capturing the local optimum solution near the starting initial point. To implement the SQP, the "fmincon" function provided by MATLAB 2021b was used. The SQP algorithm combines the objective and constraint functions into a merit function. The algorithm attempts to minimize the merit function subject to relaxed constraints. This modified problem can lead to a feasible solution. It should be also noted that the implementation of SQP in the MATLAB environment automatically calculates the gradients of the cost and gradient functions using the finite difference method when analytical gradient information is not supplied as a default option.

Thus, combining GA and SQP will result in a true global optimum solution. Repeating this procedure for many randomly generated initial points results in the same optimum solution provided in Table 5. The results of the optimization indicate that the optimal parameters (x_1, x_2, x_3, and x_4) are always those selected as lower bounds. It can be explained by considering Equations (10)–(14) and the cost function (Equation (9)) that the lower the reluctance of the magnetic circuit path, the higher the flux density that will be created in the gap. This is also implied by evaluating Hopkinson's law presented in Equation (5).

Table 5. Optimization Parameters.

Parameters	Optimized Output	Lower Bound	Upper Bound
x_1(mm)	30	30	150
x_2(mm)	25	25	60
x_3(mm)	100	100	250
x_4(mm)	20	20	250
x_5(mm)	45	30	250
x_6(mm)	0.723	0.511	2.588
Numberofturns		1838	

It is worth noting that, substituting the optimal parameters into Equation (9) yields the following simple and linear relationship between the applied current and magnetic flux density:

$$B = 0.2705I \tag{22}$$

Equation (22) is linear due to the fact that in the magnetic circuit design presented above, constant permeabilities were assumed for magnetic materials in the circuit for the sake of simplicity. In general, permeability is constant at a low applied magnetic field intensity but its value decreases as the field increases toward the saturation limit.

4. Design of the Semi-Active MRE-Based Seat Suspension

It is expected that the designed MRE-isolator will experience significant deformations between approximately 15 and 100 mm, if it is utilized independently. These deformations correspond to shear strain values ranging from 60% to about 1300%, in accordance with the physical and geometrical constraints imposed by Equation (19). To address this limitation, Figure 9 offers a design solution to develop a novel semi-active seat suspension system based on the optimally designed MRE isolator. Three passive springs are designed to be in parallel and series to the MRE isolator, as shown in Figure 9. The springs were designed to be integrated with the MRE-isolator in order to avoid an extreme deformation of MREs due to the human body dynamic. It should be noted that the inertia of the connector is assumed to be negligible. A design optimization was also formulated to obtain k_{s1} and k_{s2} in such a way that the frequency shift of the semi-active suspension system is maximized.

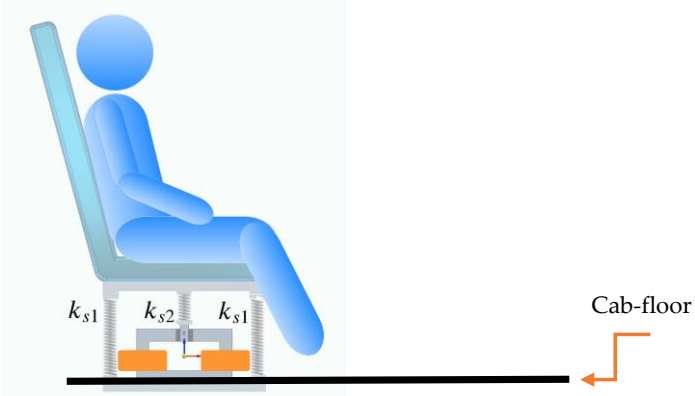

Figure 9. Schematic of the semi-active seat suspension system.

The main goals for designing the parallel-series springs integrated into the semi-active suspension are summarized as follows: (i) to allow large strokes for the suspension system while allowing the MRE to continue to operate within a reasonably low deformation (−7.5 mm~7.5 mm, corresponding to a maximum shear strain of 30%); (ii) to increase the natural frequency shift of the system when the current increases from 0 A to 2 A; and (iii) to tolerate the human body weight. Considering these design requirements, the design optimization problem can be formulated as follows:

$$\text{Minimize: } J = -(f_{n2} - f_{n1}) \tag{23}$$

where f_{n1} and f_{n2} are the natural frequency (Hz) of the seat suspension system from cab-floor to seat under the input current of 0 A and 2 A, respectively. Thus, the indices 1 and 2 in the subsequent equations denote the parameter value at zero current and maximum current of 2 A. The natural frequencies under zero and maximum currents together with the equivalent stiffness of the seat are given by the following equations:

$$f_{n1} = \frac{1}{2\pi}\sqrt{\frac{k_{eq1}}{m_{total}}} \tag{24}$$

$$f_{n2} = \frac{1}{2\pi}\sqrt{\frac{k_{eq2}}{m_{total}}} \tag{25}$$

$$k_{eq1} = k_{s1} + \left(\frac{k_{s2}k_{MRE1}}{k_{s2}+k_{MRE1}}\right) \quad (26)$$

$$k_{eq2} = k_{s1} + \left(\frac{k_{s2}k_{MRE2}}{k_{s2}+k_{MRE2}}\right) \quad (27)$$

$$\hat{x}_c \leq 7.5 \text{ mm} \quad (28)$$

where k_{eq1} and k_{eq2} are the equivalent stiffness of the suspension system under minimum and maximum input currents. It is noted that the displacement of spring k_{s1} is basically the seat displacement, as shown in Figure 9. The inequality constraint in Equation (28) is provided to ensure the displacement of the MRE isolator is limited to a maximum value of 7.5 mm (stroke of 15 mm). This can be further illuminated by Figure 8, showing an MRE operating under shear mode. It should be noted that the optimal thickness of the MRE is obtained as 25 mm, as discussed in the previous section (Table 5). Hence, the maximum shear strain of the material, $\gamma = \frac{displacement}{initial\ thickness}$ is limited to 30%. It is also worth mentioning that, according to Figure 9, the force due to spring k_{s2} should be equal to the force generated by the MREs in the electromagnet gaps.

The optimal values for the passive springs of k_{s1} and k_{s2} in the proposed adaptive seat suspension are found to be 1.006 and 50 kN/m, respectively. The optimal results together with the considered lower and upper bounds are provided in Table 6. Given the field-stiffening characteristics of MRE materials and Equations (27) and (28), along with the cost function described in Equation (24), it is anticipated that k_{s1} will tend to approach its minimum value, while k_{s2} will tend to approach its maximum value, thereby converging towards their respective lower and upper bounds. The equivalent stiffness of the optimized seat suspension system under zero current input is obtained as nearly 8.9 kN/m while under the maximum applied current of 2 A, it is increased to 17.5 kN/m. This corresponds to an absolute and relative increase of 8.6 kN/m and 96%, respectively. The natural frequency of the optimal adaptive seat suspension system varies from 1.76 Hz at zero current to 2.27 Hz at the maximum current of 2 A (29% relative frequency shift).

Table 6. Optimized values of parameters in MRE isolator design.

Stiffness	Optimization Result	Lower Bound	Upper Bound
k_{s1}(N/m)	1006	1000	50,000
k_{s2}(N/m)	50,000	1000	50,000

Performance Evaluation of the Proposed Semi-Active Seat Suspension

This section presents the vibration transmissibility of the proposed seat suspension systems considering a seated human body model. Figure 10 shows the proposed 6-DOF lumped parameter model of the coupled seated human on a suspension system equipped with an MRE isolator. The 4-DOF human body lumped parameter proposed by Wan. Y [31] is adopted in this research study. This model incorporates various components such as the head, neck, upper torso, viscera, and lower torso with a combined mass of 60.67 kg. Nonetheless, future research could investigate the variation of human body weight on the effectiveness of the suggested semi-active MRE-based seat suspension system. The mechanical response of the human body to vibrations is represented in this model using equivalent mechanical elements, namely, mass, spring, and damping. It is noted that in Figure 10, parameters m_1, m_2, m_3, m_4 are, respectively, the mass of the lower torso, viscera, upper torso, and head/neck, and k_1, k_2, k_3, k_4 as well as c_1, c_2, c_3, c_4 are the corresponding stiffness and damping of the above-mentioned parts of the human body.

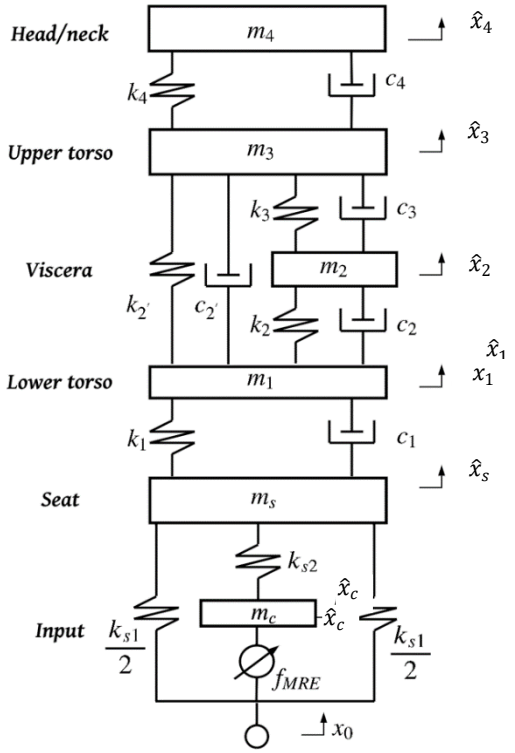

Figure 10. 6-DOF Lumped parameter model of seated human suspension system with MRE isolator.

Coordinates $\hat{x}_1, \hat{x}_2, \hat{x}_3, \hat{x}_4, \hat{x}_s$, and $\hat{x}_c$ are the displacement of the center of gravity of the lower torso, viscera, upper torso, head/neck, seat, and the isolator's connector, respectively. $\hat{x}_0$ denotes the displacement excitation to the seat suspension system. Thus, the governing equations of the motion of the 6-DOF coupled seated human/semi-active seat suspension system, as shown in Figures 8 and 10, can be derived as follows:

$$m_4\ddot{x}_4 = k_4(x_3 - x_4) + c_4(\dot{x}_3 - \dot{x}_4) \tag{29}$$

$$m_3\ddot{x}_3 = k_{2\prime}(x_1 - x_3) + c_{2\prime}(\dot{x}_1 - \dot{x}_3) + k_3(x_2 - x_3) + c_3(\dot{x}_2 - \dot{x}_3) - k_4(x_3 - x_4) - c_4(\dot{x}_3 - \dot{x}_4) \tag{30}$$

$$m_2\ddot{x}_2 = k_2(x_1 - x_2) + c_2(\dot{x}_1 - \dot{x}_2) - k_3(x_2 - x_3) - c_3(\dot{x}_2 - \dot{x}_3) \tag{31}$$

$$m_1\ddot{x}_1 = k_1(x_s - x_1) + c_1(\dot{x}_s - \dot{x}_1) - k_{2\prime}(x_1 - x_3) - c_{2\prime}(\dot{x}_1 - \dot{x}_3) - k_2(x_1 - x_2) - c_2(\dot{x}_1 - \dot{x}_2) \tag{32}$$

$$m_s\ddot{x}_s = k_{s1}(x_0 - x_s) + k_{s2}(x_c - x_s) - k_1(x_s - x_1) - c_1(\dot{x}_s - \dot{x}_1) \tag{33}$$

$$m_c\ddot{x}_c = -k_{s2}(x_c - x_s) + k_{MRE}(x_0 - x_c) + c_{MRE}(\dot{x}_0 - \dot{x}_c) \tag{34}$$

The total mass of the seat and seated human are considered to be 15 kg and 60.67 kg, respectively. The total mass of the MRE isolator's connector (nearly 100 g) is considered to be negligible. The parameters of the 4-DOFs human body lumped model are presented in Table 7.

Table 7. Parameter values of human body model [30].

m_1 (kg)	m_2 (kg)	m_3 (kg)	m_4 (kg)	
36	5.5	15	4.17	
k_1 N/m	k_2 N/m	k'_2 N/m	k_3 N/m	k_4 N/m
49,341.6	20,000	192,000	10,000	134,400
c_1N·s/m	c_2 N·s/m	c'_2 N·s/m	c_3 N·s/m	c_4 N·s/m
2475	330	909.09	200	250

Equations (29)–(34) can be formulated in matrix format in the frequency domain using Fourier-transform assuming a periodic waveform for the input displacement as follows:

$$-\omega^2[M]\{x(j\omega)\} + j\omega[C]\{x(j\omega)\} + [\mathrm{K}]\{\mathrm{x(j\omega)}\} = [\mathrm{B}]\{\mathrm{Q(\omega)}\} \tag{35}$$

$$Q(\omega) = \begin{bmatrix} 1 \\ (j\omega) \end{bmatrix}\{x_0(\omega)\} \tag{36}$$

and a displacement vector of the lumped masses as follows:

$$\{x(j\omega)\} = [x_4(j\omega), x_3(j\omega), x_2(j\omega), x_1(j\omega), x_s(j\omega)] \tag{37}$$

Let us assume:

$$[A] = -\omega^2[M] + j\omega[C] + [K] \tag{38}$$

Thus, one can write:

$$[A]\{x(j\omega)\} = [B]\{Q(\omega)\} \tag{39}$$

and solving for $x(j\omega)$ yields:

$$\{x(j\omega)\} = [A]^{-1}[B]\{Q(\omega)\} \tag{40}$$

$$\{x(j\omega)\} = [A]^{-1}[B]\begin{bmatrix} 1 \\ (j\omega) \end{bmatrix}\{x_0(\omega)\} \tag{41}$$

Therefore, the general transfer function of the coupled human body/seat response can be written as follows:

$$H(\omega) = [H_4(\omega), H_3(\omega), H_2(\omega), H_1(\omega), H_s(\omega),]^T = [A]^{-1}[B]\begin{bmatrix} 1 \\ (j\omega) \end{bmatrix} \tag{42}$$

Thus, the cab-floor-to-head acceleration transmissibility can subsequently be described as follows:

$$S(\omega) = \frac{\{x_4(j\omega)\}}{x_0(j\omega)} = H_4(\omega) \tag{43}$$

The results for the acceleration transmissibility from the cab floor to the operator's head for different currents are presented in Figure 11. As can be observed from Figure 11, when there is no suspension, the human's head receives higher levels of acceleration transmissibility as compared to with the presence of suspension. Moreover, when a higher current is applied to the MRE, the position of the transmissibility shifts to the right, thereby lowering the transmissibility and thus improving the comfort for the human.

The examination of the results presented in Figure 11 further shows that in the frequency range of 4–10 Hz where the human shows the maximum sensitivity, the transmitted acceleration is significantly reduced by the adaptive seat suspension compared with no suspension. For instance, under zero current the acceleration transmissibility obtained was nearly 4.8, while under the maximum applied current of 2 A, the magnitude of the peak resonance obtained was 3.75, showing a reduction of 21%. This confirms that the system is successful in attenuating the vibrations experienced by the occupant, leading to improved comfort and reduced potential for adverse effects caused by vibrations in that specific frequency range.

As explained in the introduction, most previous works have focused on designing MRE-based seats for horizontal vibration attenuation, and only a limited number of studies have analyzed the vertical mode MRE seat design for the purpose of whole-body vibration. Nonetheless, Li et al. [21] simulated an MRE seat isolator working in vertical mode. Although the designed isolator can attenuate the vibration transmissibility by 44%, their simulation results were obtained under the assumption that the effective MRE stiffness is

ten times greater than the scaled MRE isolator stiffness, which may not be appropriate in practice. As opposed to [21], here we proposed a practical design and implementation of a design optimization of a full-scale MRE-based semi-active seat suspension system.

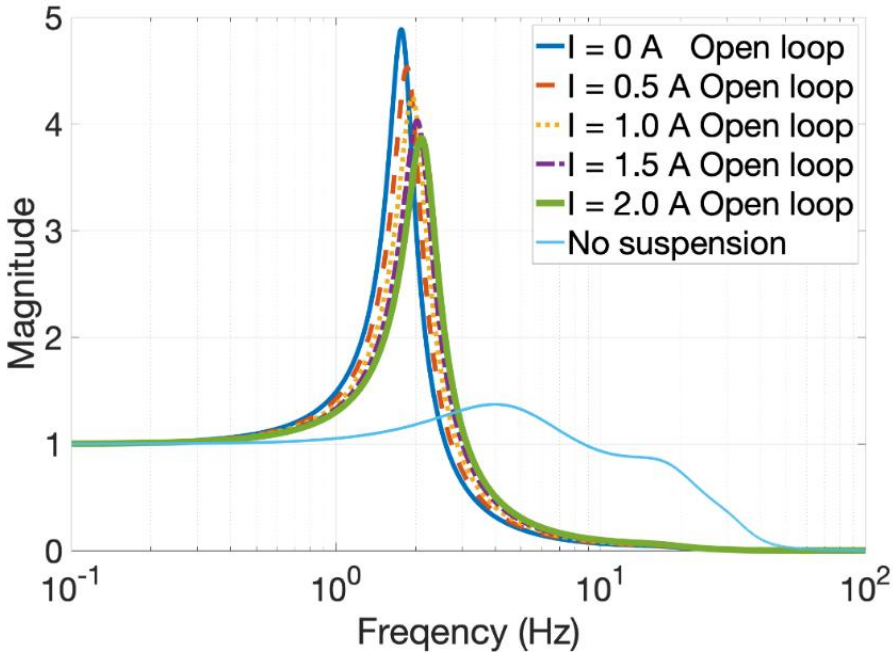

Figure 11. Acceleration transmissibility from cab floor to operator's head for different currents.

5. Conclusions

This paper presents the design development of a novel semi-active vertical mode seat suspension system that incorporates an MRE vibration isolator with a C-shaped core, accompanied by three passive parallel-series springs. The proposed configuration allowed for a large stroke while preventing the MRE from operating under excessive deformation. To optimize the design of the MRE isolator, isotropic MRE samples were fabricated and characterized using a magneto-rheometer in shear mode. The elastic and loss moduli of the MREs were then determined and modeled as functions of the loading frequency and applied magnetic flux density. The developed model facilitated the design optimization of the proposed seat suspension system to maximize the frequency shift of the seat isolator under maximum current given the important design constraints (tolerating the human body weight, and penalizing the MRE to operate in a large deformation regime). The vibration transmissibility of the proposed seat system was evaluated considering a 6-DOF lumped parameter model of the coupled seated human suspension system, incorporating the MRE isolator. The results showed that the proposed seat suspension system can adjust its natural frequency from 1.76 Hz at 0 A to 2.27 Hz at 2 A, resulting in a relative frequency shift of 29%. The analysis of the acceleration transmissibility results was indicative of a reduction in the magnitude of the peak resonance by 21% when the current increased from 0 to 2 A. The results also suggest that the proposed semi-active suspension system can effectively mitigate and diminish vibrations within this critical frequency range. These findings also provide valuable insights for the development of advanced control algorithms to regulate MRE properties in the presence of external loadings and disturbances. Future work could explore the use of artificial intelligence in developing a seat model considering wide ranges of the human body (i.e., different weights and postures) and MRE characteristics (i.e., anisotropic MRE) to improve the performance of the proposed semi-active MRE-based seat suspension system. The design of MRE seats capable of attenuating vibrations in both vertical and horizontal modes should also be investigated.

Author Contributions: Y.W.: Methodology, Software, Validation, Formal analysis, Investigation, Data curation, Writing—original draft, Visualization. H.V.: Validation, Investigation, Software, Data curation, Writing—review & editing. R.S.: Conceptualization, Methodology, Writing—review & editing, Supervision, Project administration, Funding acquisition. All authors have read and agreed to the published version of the manuscript.

Funding: Funding (under grant no. RGPIN-2021-03482) from Natural Sciences and Engineering Research Council of Canada (NSERC) is gratefully acknowledged.

Data Availability Statement: Data will be available upon request.

Acknowledgments: Support from the Natural Science and Engineering Research Council of Canada (NSERC) is gratefully acknowledged.

Conflicts of Interest: The authors declare no conflict of interest.

References

1. Heidarian, A.; Wang, X. Review on Seat Suspension System Technology Development. *Appl. Sci.* **2019**, *9*, 2834. [CrossRef]
2. Rakheja, S.; Dewangan, K.N.; Dong, R.G.; Marcotte, P. Whole-Body Vibration Biodynamics—A Critical Review: I. Experimental Biodynamics. *Int. J. Veh. Perform.* **2020**, *6*, 1–51. [CrossRef]
3. Singh, H.J.; Wereley, N.M. Biodynamic Model of a Seated Occupant Exposed to Intense Impacts. *AIAA J.* **2015**, *53*, 426–435. [CrossRef]
4. Nishiyama, K.; Harada, N.; Tsujimura, H.; Ishitake, T.; Sakakibara, H.; Matsumoto, Y. Relatedness of Occupational Exposure to Whole-Body Vibration and Health, Principally Back Symptoms. *Sangyo Eiseigaku Zasshi* **2012**, *54*, 121–140. [CrossRef] [PubMed]
5. Burström, L.; Nilsson, T.; Wahlström, J. Whole-Body Vibration and the Risk of Low Back Pain and Sciatica: A Systematic Review and Meta-Analysis. *Int. Arch. Occup. Environ. Health* **2015**, *88*, 403–418. [CrossRef] [PubMed]
6. Bai, X.-X.; Jiang, P.; Qian, L.-J. Integrated Semi-Active Seat Suspension for Both Longitudinal and Vertical Vibration Isolation. *J. Intell. Mater. Syst. Struct.* **2017**, *28*, 1036–1049. [CrossRef]
7. Behrooz, M.; Wang, X.; Gordaninejad, F. Performance of a New Magnetorheological Elastomer Isolation System. *Smart Mater. Struct.* **2014**, *23*, 045014. [CrossRef]
8. Zhao, J.; Liu, P.; Leng, D.; Zhan, H.; Luan, G.; Ning, D.; Yu, J. Prescribed Performance Control-Based Semi-Active Vibration Controller for Seat Suspension Equipped with an Electromagnetic Damper. *Vibration* **2023**, *6*, 303–318. [CrossRef]
9. Zhang, H.; Cheng, K.; Wang, E.; Rakheja, S.; Su, C.-Y. Nonlinear Behaviors of a Half-Car Magneto-Rheological Suspension System under Harmonic Road Excitation. *IEEE Trans. Veh. Technol.* **2023**, *72*, 8592–8600. [CrossRef]
10. Zhu, M.; Lv, G.; Zhang, C.; Jiang, J.; Wang, H. Delay-Dependent Sliding Mode Variable Structure Control of Vehicle Magneto-Rheological Semi-Active Suspension. *IEEE Access* **2022**, *10*, 51128–51141. [CrossRef]
11. Gągorowski, A. Controlling the Magnetorheological Suspension of a Vehicle Seat Including the Biomechanics of the Driver. *Cent. Eur. J. Eng.* **2012**, *2*, 264–278. [CrossRef]
12. Lin, Y.; Liu, C.; Wen, G.; Sedaghati, R. A Semi-Active Quasi-Zero Stiffness Vibration Isolator Based on Magnetorheological Elastomer with a Fast Convergence Switch Control. *J. Intell. Mater. Syst. Struct.* **2023**, *34*, 1045389X221147628. [CrossRef]
13. Snyder, R.A.; Kamath, G.M.; Wereley, N.M. Characterization and Analysis of Magnetorheological Damper Behavior Under Sinusoidal Loading. *AIAA J.* **2001**, *39*, 1240–1253. [CrossRef]
14. Ngatu, G.T.; Hu, W.; Wereley, N.M.; Kothera, C.S. Adaptive Snubber-Type Magnetorheological Fluid-Elastomeric Helicopter Lag Damper. *AIAA J.* **2010**, *48*, 598–610. [CrossRef]
15. Abdalaziz, M.; Sedaghati, R.; Vatandoost, H. Development of a New Dynamic Hysteresis Model for Magnetorheological Dampers with Annular-Radial Gaps Considering Fluid Inertia and Compressibility. *J. Sound Vib.* **2023**, *561*, 117826. [CrossRef]
16. Dushchenko, V.V.; Masliev, V.G.; Nanivskyi, R.A.; Masliev, A.O. Application of magnetorheological elastomers for performance control of cushioning systems for wheeled vehicles. *Electr. Eng. Electromechan.* **2019**, *5*, 50–59. [CrossRef]
17. Le, T.D.; Ahn, K.K. A Vibration Isolation System in Low Frequency Excitation Region Using Negative Stiffness Structure for Vehicle Seat. *J. Sound Vib.* **2011**, *330*, 6311–6335. [CrossRef]
18. Sun, S.; Yang, J.; Deng, H.; Du, H.; Li, W.; Alici, G.; Nakano, M. Horizontal Vibration Reduction of a Seat Suspension Using Negative Changing Stiffness Magnetorheological Elastomer Isolators. *Int. J. Veh. Des.* **2015**, *68*, 104–118. [CrossRef]
19. Choi, Y.; Wereley, N.M. Vibration Isolation Performance of an Adaptive Magnetorheological Elastomer-Based Dynamic Vibration Absorber. *Actuators* **2022**, *11*, 157. [CrossRef]
20. Choi, Y.T.; Wereley, N.M. Adaptively Tunable Magnetorheological Elastomer-Based Vibration Absorber for a Propeller Aircraft Seat. *AIP Adv.* **2022**, *12*, 035332. [CrossRef]
21. Li, W.; Zhang, X.; Du, H. Development and Simulation Evaluation of a Magnetorheological Elastomer Isolator for Seat Vibration Control. *J. Intell. Mater. Syst. Struct.* **2012**, *23*, 1041–1048. [CrossRef]
22. Du, H.; Li, W.; Zhang, N. Semi-Active Variable Stiffness Vibration Control of Vehicle Seat Suspension Using an MR Elastomer Isolator. *Smart Mater. Struct.* **2011**, *20*, 105003. [CrossRef]

23. Liu, C.; Hemmatian, M.; Sedaghati, R.; Wen, G. Development and Control of Magnetorheological Elastomer-Based Semi-Active Seat Suspension Isolator Using Adaptive Neural Network. *Front. Mater.* **2020**, *7*, 171. [CrossRef]
24. Carrella, A.; Brennan, M.J.; Waters, T.P. Static Analysis of a Passive Vibration Isolator with Quasi-Zero-Stiffness Characteristic. *J. Sound Vib.* **2007**, *301*, 678–689. [CrossRef]
25. Vatandoost, H.; Hemmatian, M.; Sedaghati, R.; Rakheja, S. Dynamic Characterization of Isotropic and Anisotropic Magnetorheological Elastomers in the Oscillatory Squeeze Mode Superimposed on Large Static Pre-Strain. *Compos. Part B Eng.* **2020**, *182*, 107648. [CrossRef]
26. Böse, H.; Gerlach, T.; Ehrlich, J. Magnetorheological elastomers—An underestimated class of soft actuator materials. *J. Intell. Mater. Syst. Struct.* **2021**, *32*, 1550–1564. [CrossRef]
27. Vatandoost, H.; Rakheja, S.; Sedaghati, R.; Hemmatian, M. Compensation of Magnetic Force of an Electromagnet for Compression Mode Characterization of Magnetorheological Elastomers. *IEEE Trans. Magn.* **2020**, *57*, 2500114. [CrossRef]
28. Vatandoost, H.; Sedaghati, R.; Rakheja, S. A Novel Methodology for Accurate Estimation of Magnetic Permeability of Magnetorheological Elastomers. *J. Magn. Magn. Mater.* **2022**, *560*, 169669. [CrossRef]
29. ISO 2631-1:1997; Mechanical Vibration and Shock—Evaluation of Human Exposure to Whole-Body Vibration—Part 1: General Requirements. Available online: https://www.iso.org/standard/7612.html (accessed on 1 May 1997).
30. Wan, Y.; Schimmels, J.M. Optimal Seat Suspension Design Based on Minimum "Simulated Subjective Response". *J. Biomech. Eng.* **1997**, *119*, 409–416. [CrossRef]
31. Wan, Y.; Schimmels, J.M. A Simple Model That Captures the Essential Dynamics of a Seated Human Exposed to Whole Body Vibration. *Adv. Bioeng.* **1995**, *31*, 333–334.

Disclaimer/Publisher's Note: The statements, opinions and data contained in all publications are solely those of the individual author(s) and contributor(s) and not of MDPI and/or the editor(s). MDPI and/or the editor(s) disclaim responsibility for any injury to people or property resulting from any ideas, methods, instructions or products referred to in the content.